Monthly Notices
of the
ROYAL ASTRONOMICAL SOCIETY
MNRAS **440,** 1999–2012 (2014) doi:10.1093/mnras/stu413

Herschel *-ATLAS: deep *HST*/WFC3 imaging of strongly lensed submillimetre galaxies

M. Negrello,[1†] R. Hopwood,[2] S. Dye,[3] E. da Cunha,[4] S. Serjeant,[5] J. Fritz,[6] K. Rowlands,[7] S. Fleuren,[8] R. S. Bussmann,[9,10] A. Cooray,[11] H. Dannerbauer,[12] J. Gonzalez-Nuevo,[13] A. Lapi,[14,15] A. Omont,[16,17] S. Amber,[5] R. Auld,[18] M. Baes,[6] S. Buttiglione,[1] A. Cava,[19] L. Danese,[15] A. Dariush,[18] G. De Zotti,[1,15] L. Dunne,[20] S. Eales,[18] E. Ibar,[21] R. J. Ivison,[22,23] S. Kim,[24] L. Leeuw,[25] S. Maddox,[20] M. J. Michałowski,[23] M. Massardi,[26] E. Pascale,[18] M. Pohlen,[18] E. Rigby,[27] D. J. B. Smith,[28] W. Sutherland,[8] P. Temi[29] and J. Wardlow[11]

Affiliations are listed at the end of the paper

Accepted 2014 February 28. Received 2014 February 28; in original form 2013 November 22

ABSTRACT

We report on deep near-infrared observations obtained with the Wide Field Camera-3 (WFC3) onboard the *Hubble Space Telescope* (*HST*) of the first five confirmed gravitational lensing events discovered by the *Herschel* Astrophysical Terahertz Large Area Survey (H-ATLAS). We succeed in disentangling the background galaxy from the lens to gain separate photometry of the two components. The *HST* data allow us to significantly improve on previous constraints of the mass in stars of the lensed galaxy and to perform accurate lens modelling of these systems, as described in the accompanying paper by Dye et al. We fit the spectral energy distributions of the background sources from near-IR to millimetre wavelengths and use the magnification factors estimated by Dye et al. to derive the *intrinsic* properties of the lensed galaxies. We find these galaxies to have star-formations rates (SFR) $\sim$ 400–2000 $M_\odot$ yr^{-1}, with $\sim$(6–25) $\times$ 10^{10} $M_\odot$ of their baryonic mass already turned into stars. At these rates of star formation, all remaining molecular gas will be exhausted in less than $\sim$100 Myr, reaching a final mass in stars of a few 10^{11} $M_\odot$. These galaxies are thus proto-ellipticals caught during their major episode of star formation, and observed at the peak epoch ($z \sim 1.5$–3) of the cosmic star formation history of the Universe.

Key words: gravitational lensing: strong – galaxies: elliptical and lenticular, cD – galaxies: evolution – galaxies: formation – infrared: galaxies – submillimetre: galaxies.

1 INTRODUCTION

Recent evidence indicate that almost all of high-redshift ($z \gtrsim 1$) dust-obscured star-forming galaxies selected in the sub-millimetre (hereafter sub-mm galaxies, or SMGs) with flux density above $\sim$100 mJy at 500 μm are gravitationally lensed by a foreground galaxy or a group/cluster of galaxies (Negrello et al. 2010, hereafter N10; Conley et al. 2011; Cox et al. 2011; Bussmann et al. 2013; Fu et al. 2012; Wardlow et al. 2013). These sub-mm bright sources are rare, their surface density being $\lesssim$0.3 deg^{-2} at $F_{500} \gtrsim 100$ mJy (Negrello et al. 2007) and therefore only detectable in wide-area sub-mm surveys. In fact, sub-mm surveys before the advent of the *Herschel* Space Observatory (Pilbratt et al. 2010) were either limited to small areas of the sky (i.e. <1 deg^2) or severely affected by source confusion due to poor spatial resolution (e.g. Coppin et al. 2006; Devlin et al. 2009; Weiss et al. 2009).

The *Herschel* Astrophysical Terahertz Large Area Survey[1] (H-ATLAS) (Eales et al. 2010a) is the widest area extragalactic survey undertaken with *Herschel*. It has mapped $\sim$570 deg^2 in five bands

∗ *Herschel* is an ESA space observatory with science instruments provided by European-led Principal Investigator consortia and with important participation from NASA.

† E-mail: mattia.negrello@oapd.inaf.it

[1] www.h-atlas.org

from 100 to 500 μm, down to around the 250–500 μm confusion limit. The first 16 deg^2 were observed during the Science Demonstration Phase (SDP) and detected 10 extragalactic sources with $F_{500} \geq 100$ mJy. Existing shallow optical and radio data clearly identify four of these as low redshift (i.e. $z < 0.1$) spiral galaxies (Baes et al. 2010) and one as a radio bright ($F_{1.4\,\mathrm{GHz}} > 100$ mJy) blazar at $z = 1$ (Gonzalez-Nuevo et al. 2010), while the remaining five have sub-mm colours (i.e. 250 μm/350 μm versus 350 μm/500 μm flux ratios) indicative of dusty star-forming galaxies at $z > 1$. If SMGs have a steep luminosity function, as several models suggest (Granato et al. 2004; Lapi et al. 2006) and recent results support (Eales et al. 2010b; Lapi et al. 2011; Gruppioni et al. 2013), their number counts are expected to exhibit a sharp cut-off at bright fluxes ($\simeq$80–100 mJy at 500 μm). This cut-off implies that only SMGs that have had their flux boosted by an event of gravitational lensing can be detected above this brightness threshold (Negrello et al. 2007, see also fig. 1 of N10).

To test this prediction, the five sources with $F_{500} > 100$ mJy and with high-z colours identified in the H-ATLAS/SDP field have been the subject of intensive multiwavelength follow-up observations. The follow-up campaign includes observations from the ground with the Keck telescopes (N10), the Submillimetre Array (SMA) (Bussmann et al. 2013; N10), the Zpectrometer instrument on the NRAO Robert C. Byrd Green Bank Telescope (GBT) (Frayer et al. 2011; Harris et al. 2012), the Z-Spec spectrometer (Lupu et al. 2012), the IRAM Plateau de Bure Interferometer (PdBI) (Omont et al. 2011, 2013; George et al., in preparation), the Max-Planck Millimeter Bolometer (MAMBO) at the IRAM 30 m telescope on Pico Veleta (Dannerbauer et al., in preparation), the Combined Array for Research in Millimeter-wave Astronomy (CARMA) (Leew et al., in preparation), the Jansky Very Large Array (JVLA; Ivison et al., in preparation) and also from space with the *Spitzer* Space Telescope (Hopwood et al. 2011) and the *Herschel*/SPIRE Fourier Transform Spectrometer (Valtchanov et al. 2011). The detection, in these objects, of carbon monoxide (CO) rotational line emission, which is a tracer of molecular gas associated with star-forming environments, has provided redshifts in the range $z \sim 1.5$–3, consistent with what can be inferred from their sub-mm colours (N10). In contrast, the same sources are closely aligned with lower redshift ($z < 1$) galaxies detected in the Sloan Digital Sky Survey (SDSS) (Smith et al. 2011) and in the VISTA Kilo-degree INfrared Galaxy (VIKING) Survey (Fleuren et al. 2012), thus confirming the presence of a foreground galaxy acting as a lens. In four of these systems the background galaxy has been clearly resolved into multiple images at 880 μm with the SMA (N10; Bussmann et al. 2013) thus providing the definitive confirmation of the lensing hypothesis. As part of this extensive follow-up campaign we obtained observations in the near-IR with the Wide Field Camera-3 (WFC3) onboard the *Hubble Space Telescope* (*HST*) during cycle-18, using the wide-J filter F110W and the wide-H filter F160W.

In this paper, we report on the results of these observations. We exploit the sub-arcsecond spatial resolution and sensitivity of the *HST* observations to disentangle the background source from the foreground galaxy to constrain the near-IR emission of the two components separately. A detailed lens modelling of these systems using a 'semilinear inversion approach' is presented in an accompanying paper (Dye et al. 2014, hereafter D14). The work is organized as follows. In Section 2 we present the *HST* data. In Section 3 we discuss other ancillary data used to build the panchromatic spectral energy distribution (SED) of the sources. The subtraction of the foreground lens and the measurement of the photometry of the lens and the background galaxy are discussed in Section 4. A fit to the SED of the lensed galaxy, from optical to millimetre wavelength, with the addition of the near-IR *HST* points, is performed in Section 5. The results are discussed in Section 6 while Section 7 summarizes the main conclusions.

Table 1. Total exposure times for observations taken with *HST*/WFC3 using the F110W and F160W filters.

H-ATLAS ID	F110W (s)	F160W (s)
SDP.9	1412	3718
SDP.11	1412	3718
SDP.17	1412	3718
SDP.81	712	4418
SDP.130	712	4418

2 *HST* DATA

HST observations of the five lens candidates presented in N10 were taken in 2011 April as part of the cycle-18 proposal 12194 (PI: Negrello) using 10 orbits in total, two for each target. Observations were made with the WFC3 using the wide-J filter F110W (peak wavelength 1.15 μm) and the wide-H filter F160W (peak wavelength 1.545 μm), in order to maximize the chance of detection of the background galaxy, whose emission at shorter wavelengths is expected to be dominated by the foreground galaxy. About one and a half orbits were dedicated to observations in the *H* band with only half an orbit (or less) spent for observations with the F110W filter. This relatively short exposure was aimed at revealing the morphology of the lens, with minimal contamination from the background source. The total exposure times are reported in Table 1. Data were reduced using the IRAF MultiDrizzle package. The pixel scale of the Infrared-Camera is 0.128 arcsec but we resampled the images to a finer pixel scale of 0.064 arcsec by exploiting the adopted dither strategy (a sub-pixel dither patter). This provides us with a better sampling of the point spread function (PSF) whose full width at half-maximum (FWHM) is ∼0.13–0.16 arcsec at wavelengths $\lambda = 1.1$–1.6 μm. Cosmic ray rejections and alignments of the individual frames were also addressed before combining and rebinning the images. Multidrizzle parameters were optimized to the final image quality. *HST* cut-outs around the five targets are shown in Fig. 1 and in the left panels of Fig. 2. Due to the relatively longer integration times, the combined F160W images exhibit higher signal-to-noise ratio than those obtained with the F110W filter; however the main features revealed in the *H* band are also captured with the shorter exposures in the *J* band.[2]

3 ANCILLARY DATA

These *HST* images represent the latest addition to the already substantial set of photometric and spectroscopic data for these sources that are reported in Table 2, and briefly summarized below.

[2] A cycle-19 *HST*/WFC3/F110W snapshot program has provided imaging data for $\gtrsim$100 lens candidates identified in *H*-ATLAS (PID: 12488; PI: Negrello).

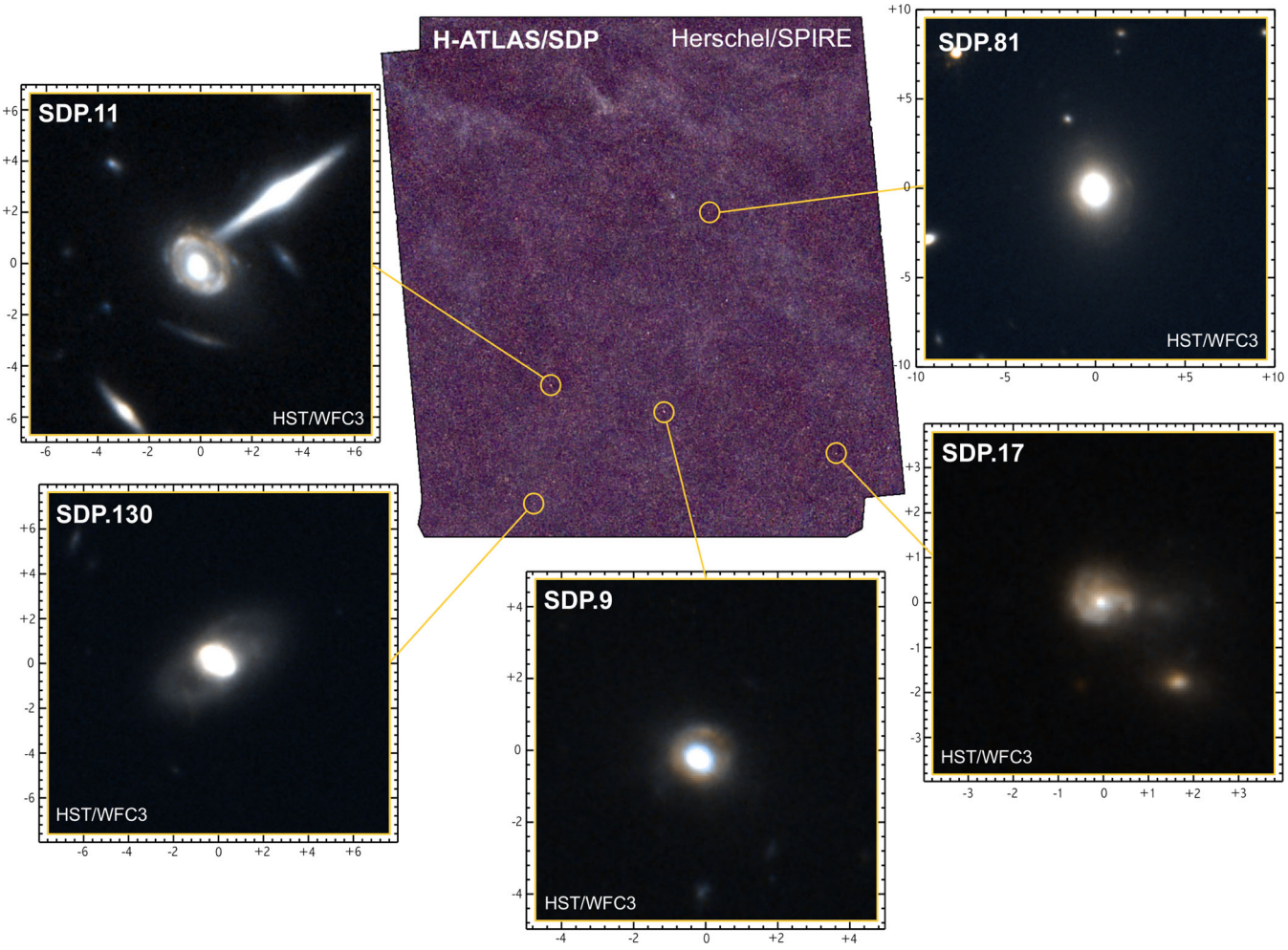

Figure 1. Two-colour postage stamp *HST*/WFC3 images of the first five confirmed gravitational lensing systems discovered by H-ATLAS (blue for F110W and red for F160W). The position of the five sources in the *Herschel*/SPIRE map of the H-ATLAS SDP field is indicated by the yellow circles. The scale of the postage stamps is given in arcseconds.

3.1 Far-infrared and sub-mm/mm

Flux density estimates at 100 to 500 μm are provided by *Herschel*/PACS (Poglitsch et al. 2010) and *Herschel*/SPIRE (Griffin et al. 2010), which are used in parallel mode for *H*-ATLAS. A description of the map-making for the PACS and SPIRE data of the *H*-ATLAS/SDP field can be found in Ibar et al. (2010) and Pascale et al. (2010), respectively, while details of the source extraction and flux measurements are given in Rigby et al. (2011). The achieved $5\,\sigma$ detection limits (including source confusion) are 33.5 to 44.0 mJy/beam from 250 to 500 μm, 132 mJy/beam at 100 μm and 121 mJy/beam at 160 μm. The five sources discussed here have, by selection, a flux density above 100 mJy at 500 μm (see Table 2) and are therefore robustly detected at the SPIRE wavebands. However only three of them are detected in PACS at more than 3σ, namely SDP.9, SDP.11 and SDP.17. One source, SDP.81, was undetected while the other, SDP.130, falls outside the region covered by PACS in parallel mode. Deeper PACS minimaps of these two objects at 70 μm and 160 μm were obtained by Valtchanov et al. (2011). Both sources were detected at 160 μm while upper limits on their flux density were obtained at 70 μm.

Follow-up observations with the SMA (N10; Bussmann et al. 2013) and IRAM/MAMBO (N10; Dunnerbauer et al., in preparation) provide flux estimates for all five targets at 880 μm and at 1200 μm, respectively.

3.2 Optical

The *H*-ATLAS/SDP field is covered by the SDSS. Four of the H-ATLAS/SDP lenses have a reliable association in SDSS with $r < 22.40$ (Smith et al. 2011), the exception being SDP.11, whose optical counterpart has $r = 22.41$. The SDSS flux densities used for the SED fitting in Section 5 are those derived from the Data Release 7 model magnitudes (see also N10).

Dedicated follow-up observations with the Keck telescope provided supplementary optical imaging in the *g* and *i* bands. As discussed in N10, the lensed sources are undetected in the optical. The optical flux densities reported in Table 2, derived from the light-profile modelling as described in N10, refer to either the whole system (lens+source) or the lens alone when the latter is completely dominating over the background galaxy as suggested by the *HST* imaging data. Upper limits on the optical emission from the background source are also shown in the table. These limits were derived after subtracting the best-fitting model for the light profile. The local standard deviation was scaled to the area of a ring of radius

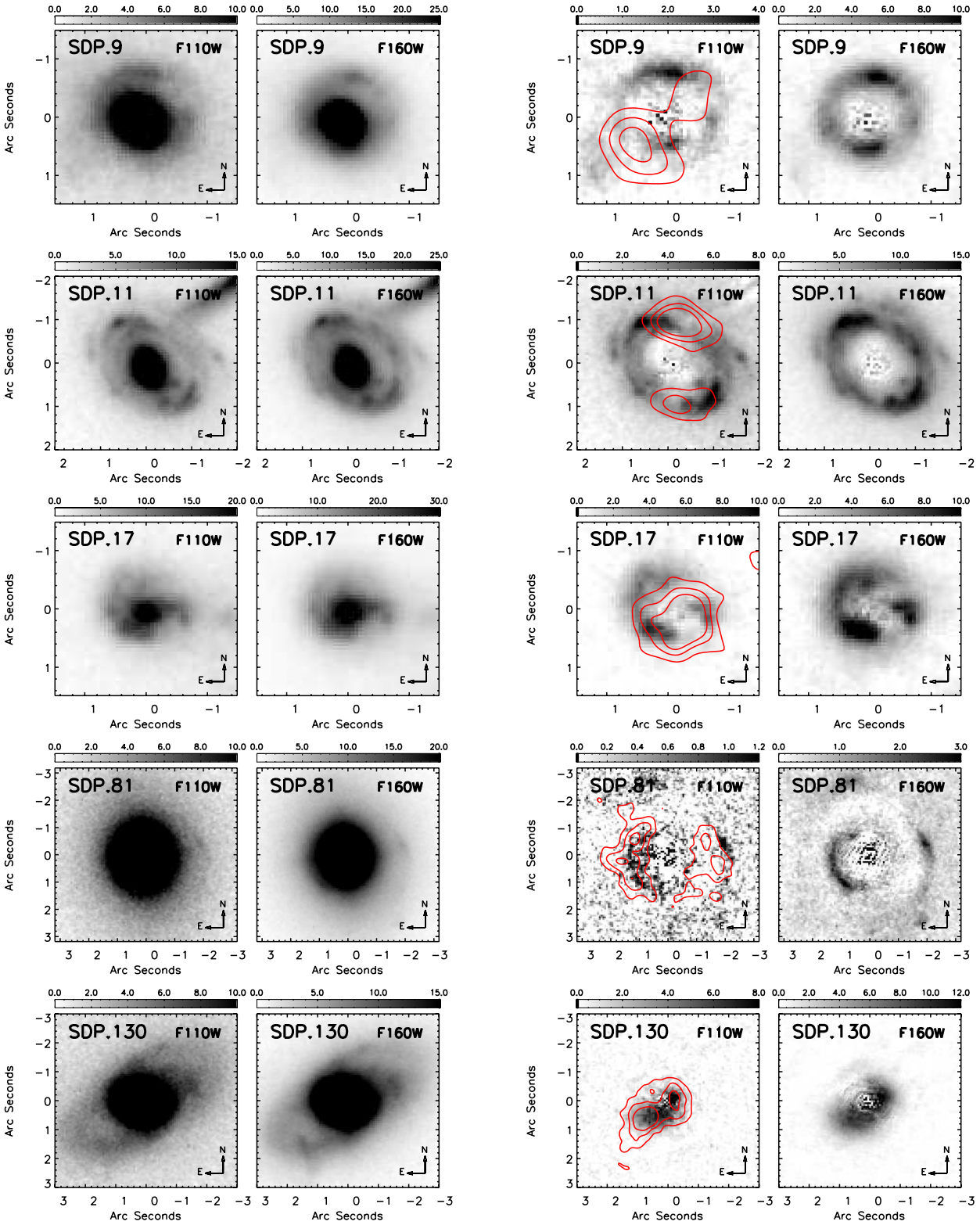

Figure 2. *HST*/WFC3 images taken with the F110W and the F160W filters (left panels) of the first gravitational lensing events discovered by H-ATLAS (N10). The corresponding lens subtracted images are shown in the right panels. The colour code represents the surface brightness in μJy arcsec^{-2}. Signal-to-noise ratio contours at 880 μm from the SMA (Bussmann et al. 2013) are shown against the lens subtracted F110W images (red curves, in steps of 3, 6 and 9).

Table 2. Photometric data, spectroscopic redshifts and best-fitting SED parameters for the lens and for the background source. At those wavelengths where the separation between the foreground galaxy and the background source was not possible, the total (lens+source) photometry is provided. All the errors correspond to the 68 per cent confidence interval. Unless otherwise indicated, the data come from N10.

IAU name	SDP.9 J090740.0−004200	SDP.11 J091043.1−000321	SDP.17 J090302.9−014127	SDP.81 J090311.6+003906	SDP.130 J091305.0−005343
Lens					
Keck g (μJy)	1.50 ± 0.23	1.54 ± 0.20	...	66.0 ± 14	18.4 ± 2.7
Keck i (μJy)	21.5 ± 2.6	23.8 ± 1.9	...	105 ± 21	93.7 ± 0.9
SDSS u (μJy)	0.24 ± 0.23	0.57 ± 0.58	...	3.9 ± 2.0	1.7 ± 1.7
SDSS g (μJy)	1.79 ± 0.43	1.01 ± 0.45	...	24.9 ± 1.1	19.4 ± 0.7
SDSS r (μJy)	5.81 ± 0.70	3.94 ± 0.65	...	115 ± 2	66.1 ± 1.2
SDSS i (μJy)	14.9 ± 1.1	11.3 ± 1.0	...	198 ± 4	109 ± 2
SDSS z (μJy)	27.0 ± 3.7	...	...	278 ± 8	143 ± 7
HST/F110W (μJy)	37.4 ± 1.6	34.6 ± 1.5	13.2 ± 1.0	273 ± 4	202 ± 61
HST/F160W (μJy)	60.3 ± 3.0	54.4 ± 2.9	19.8 ± 2.0	381 ± 8	275 ± 83
VIKING Z (μJy)	31.3 ± 1.6	...	...	210 ± 2	157 ± 2
VIKING Y (μJy)	33.0 ± 4.3	...	...	233 ± 5	196 ± 3
VIKING J (μJy)	52.0 ± 4.0	...	...	379 ± 5	244 ± 5
VIKING H (μJy)	...	...	...	485 ± 8	310 ± 9
VIKING Ks (μJy)	...	...	...	630 ± 12	388 ± 9
Spitzer 3.6 μm (μJy)[(b)]	...	...	...	354 ± 43	213 ± 30
Spitzer 4.5 μm (μJy)[(b)]	...	...	...	220 ± 40	230 ± 10
Redshift	0.6129 ± 0.0005[(a)]	0.7932 ± 0.0012	0.9435 ± 0.0009	0.2999 ± 0.0002	0.2201 ± 0.002
M_* (10^{10} $M_\odot$)	$6.8^{+1.4}_{-1.6}$	$10.1^{+2.8}_{-2.5}$	$3.9^{+1.6}_{-1.3}$	$10.3^{+2.8}_{-2.8}$	$4.2^{+1.0}_{-1.1}$
SFR ($M_\odot$ yr^{-1})	$0.19^{+0.13}_{-0.10}$	$0.77^{+0.46}_{-0.37}$	$3.3^{+1.9}_{-1.7}$	$0.25^{+0.28}_{-0.16}$	$0.06^{+0.09}_{-0.05}$
Sérsic index at F110W (n_S^{F110W})	5.1	$1.0 + 2.8$	$0.7 + 11.0$	$2.3 + 2.0$	Multiple profiles
Sérsic index at F160W (n_S^{F160W})	5.8	$1.0 + 4.5$	$0.6 + 9.7$	$2.9 + 0.9$	multiple profiles
Background source					
Keck g (μJy; 5σ upper limits)	<0.20	<0.32	...	<0.28	<0.16†
Keck i (μJy; 5σ upper limits)	<0.75	<1.2	...	<0.87	<0.53†
HST/F110W (μJy)	3.6 ± 0.5	23.8 ± 4.3	8.7 ± 1.7	1.9 ± 0.4	11.1 ± 3.3
HST/F160W (μJy)	12.3 ± 1.4	47.7 ± 6.9	16.2 ± 3.2	4.5 ± 0.8	27.1 ± 8.1
Spitzer 3.6 μm (μJy)[(b)]	...	...	...	62 ± 44	44 ± 20
Spitzer 4.5 μm (μJy)[(b)]	...	...	...	126 ± 54	47 ± 10
WISE 12 μm (mJy)	1.31 ± 0.05	2.14 ± 0.06	1.37 ± 0.05	<0.26	<0.49
WISE 22 μm (mJy)	4.2 ± 0.3	9.2 ± 0.4	5.6 ± 0.4	<1.76	<2.68
PACS 70 μm (mJy)	...	...	...	<8.0[(f)]	<9.0[(f)]
PACS 100 μm (mJy)	187 ± 57	198 ± 55	78 ± 55	<62	...
PACS 160 μm (mJy)	416 ± 94	397 ± 90	182 ± 56	51 ± 5[(f)]	45 ± 8[(f)]
SPIRE 250 μm (mJy)	485 ± 73	442 ± 67	328 ± 50	129 ± 20	105 ± 17
SPIRE 350 μm (mJy)	323 ± 49	363 ± 55	308 ± 47	182 ± 28	128 ± 20
SPIRE 500 μm (mJy)	175 ± 28	238 ± 37	220 ± 34	166 ± 27	108 ± 18
SMA 880 μm (mJy)[(a)]	24.8 ± 3.3	30.6 ± 2.4	54.7 ± 3.1	78.4 ± 8.2	36.7 ± 3.9
MAMBO 1200 μm (mJy)	7.6 ± 1.4	12.2 ± 2.3	15.3 ± 3.9	20.0 ± 3.1	11.2 ± 2.1
Redshift	1.577 ± 0.008	1.786 ± 0.005	2.3049 ± 0.0006[(c)]	3.042 ± 0.001	2.6260 ± 0.0003
μ[(d)]	$6.29^{+0.27}_{-0.26}$	$7.89^{+0.21}_{-0.25}$	$3.56^{+0.19}_{-0.17}$	$10.6^{+0.6}_{-0.7}$	$3.09^{+0.19}_{-0.17}$
$\mu^{(a)}_{SMA}$	8.8 ± 2.2	10.9 ± 1.3	4.9 ± 0.7	11.1 ± 1.1	2.1 ± 0.3
L_{dust}/μ (10^{12} $L_\odot$)	$7.4^{+1.2}_{-1.2}$	$7.6^{+1.2}_{-1.0}$	$20.7^{+4.0}_{-3.5}$	$5.1^{+0.8}_{-0.7}$	$9.2^{+1.6}_{-1.4}$
SFR/μ ($M_\odot$ yr^{-1})	366^{+441}_{-259}	650^{+157}_{-456}	2325^{+472}_{-485}	527^{+102}_{-91}	1026^{+318}_{-206}
$T^{(warm)}_{dust}$ (K)	$45.4^{+2.8}_{-2.2}$	$46.9^{+2.8}_{-2.5}$	$43.3^{+5.9}_{-3.4}$	$39.3^{+2.1}_{-1.5}$	$37.3^{+2.1}_{-1.6}$
$\xi^{(warm)}_{dust}$	$0.80^{+0.10}_{-0.10}$	$0.84^{+0.07}_{-0.08}$	$0.72^{+0.06}_{-0.07}$	$0.74^{+0.10}_{-0.10}$	$0.73^{+0.11}_{-0.11}$
M_{dust}/μ (10^8 $M_\odot$)	$6.7^{+1.2}_{-1.0}$	$6.6^{+1.1}_{-0.9}$	$28.8^{+7.0}_{-4.9}$	$10.6^{+2.9}_{-1.9}$	$22.7^{+5.8}_{-4.1}$
M_*/μ (10^{10} $M_\odot$)	$7.1^{+4.2}_{-2.3}$	$18.7^{+5.8}_{-4.5}$	$24.2^{+8.6}_{-4.0}$	$6.6^{+2.6}_{-1.9}$	$13.7^{+3.8}_{-2.5}$
M_{gas}/μ (10^{10} $M_\odot$)[(e)]	$3.4^{+1.2}_{-0.9}$	$3.0^{+1.1}_{-0.8}$	$5.9^{+2.2}_{-1.6}$	$3.3^{+1.2}_{-0.9}$	$5.3^{+2.0}_{-1.4}$
$f_{gas} = M_{gas}/(M_{gas} + M_*)$	$0.32^{+0.13}_{-0.10}$	$0.14^{+0.06}_{-0.04}$	$0.19^{+0.06}_{-0.05}$	$0.33^{+0.09}_{-0.09}$	$0.28^{+0.08}_{-0.07}$
$\tau_{gas} = M_{gas}$/SFR (Myr)	103^{+236}_{-64}	57^{+99}_{-23}	26^{+11}_{-8}	63^{+27}_{-19}	50^{+23}_{-18}
Lens + background source					
Keck g (μJy)	...	...	1.15 ± 0.23	...	...
Keck i (μJy)	...	...	9.31 ± 1.9	...	...
SDSS u (μJy)	...	...	3.3 ± 1.6	...	...
SDSS g (μJy)	...	...	3.9 ± 0.6	...	...

Table 2 – *continued.*

IAU name	SDP.9 J090740.0−004200	SDP.11 J091043.1−000321	SDP.17 J090302.9−014127	SDP.81 J090311.6+003906	SDP.130 J091305.0−005343
SDSS *r* (μJy)	...	...	7.7 ± 1.0	...	...
SDSS *i* (μJy)	...	...	15.3 ± 1.5	...	...
SDSS *z* (μJy)	...	21.5 ± 4.2	11.8 ± 6.0	...	...
VIKING *Z* (μJy)	...	40.1 ± 0.5	10.5 ± 0.5	...	...
VIKING *Y* (μJy)	...	53.5 ± 1.1	17.1 ± 1.1	...	...
VIKING *J* (μJy)	...	78.4 ± 1.1	25.0 ± 3.7	...	...
VIKING *H* (μJy)	92.4 ± 5.2	120.0 ± 2.8	34.9 ± 3.9	...	...
VIKING *Ks* (μJy)	123.2 ± 5.4	199.7 ± 2.4	74.5 ± 4.8	...	...
WISE 3.4 μm (μJy)	218.2 ± 3.9	519 ± 6.9	132.3 ± 3.9	343.2 ± 5.1	208.0 ± 4.3
WISE 4.6 μm (μJy)	300.6 ± 6.6	632 ± 10	209.1 ± 6.8	303.9 ± 6.9	233.8 ± 7.7

[(a)] From Bussmann et al. (2013); [(b)] from Hopwood et al. (2011); [(c)] from Omont et al. (2013); [(d)] from D14; [(e)] from Frayer et al. (2011, table 1, assuming a 30 per cent error) and Lupu et al. (2012, table 4, assuming a 30 per cent error); † 'tentative'.

1.5 arcsec (inner radius of 1 arcsec and outer radius of 2 arcsec). The limits are not reported for SDP.17; in fact, in this case the *HST* data suggest (Section 5) that at optical wavelengths the emission of the source might not be negligible, implying that the GALFIT model derived from the Keck image carries contributions from both the lens and the background galaxy.

3.3 Near- and mid-infrared

Near-IR imaging data are available through the UKIRT Infrared Deep Sky Survey (UKIDSS), Large Area Survey (LAS) and the VIKING (Sutherland et al., in preparation) survey (see also Fleuren et al. 2012). The VIKING survey is 1.4 mag deeper than UKIDSS/LAS, so we use VIKING data only in the present work. The VIKING survey provides photometric measurements in five broad-band filters: *Z*, *Y*, *J*, *H*, and *Ks*, down to a typical 5σ magnitude limit of 21.0 in *J* band and 19.2 in *Ks* band (in the Vega system). The median image quality is ∼0.9 arcsec. All our targets are found to have a reliable association in the VIKING survey (Fleuren et al. 2012). For SED fitting analysis we use VIKING flux densities estimated from aperture photometry with an aperture radius of 2 arcsec for SDP.9 and SDP.11, 1 arcsec for SDP.17, and 4 arcsec for SDP.81 and SDP.130. Associated errors are derived from the distribution of the flux densities values that were obtained by taking aperture photometry at random positions in the field (avoiding the region around detected sources).

For SDP.81 and SDP.130, near-IR imaging data at 3.6 and 4.5 μm are also available from *Spitzer* (Hopwood et al. 2011). At those wavelengths the emission from the lens and the background galaxy are comparable (i.e. source to lens flux density ratio $\gtrsim$0.2) and the separation of the two contributions was performed by using the information from the SMA and the Keck data as a prior (see Hopwood et al. for details).

Imaging data at 3.4, 4.6, 12 and 22 μm, with an angular resolution of 6.1 arcsec, 6.4 arcsec, 6.5 arcsec and 12.0 arcsec, respectively, are provided by the *Wide-field Infrared Survey Explorer* (*WISE*) (Wright et al. 2010) all sky survey. The *WISE* images have a $5\,\sigma$ photometric sensitivity of 0.068, 0.098, 0.86 and 5.4 mJy, respectively, in unconfused regions. Postage stamp images centred at the position of the five H-ATLAS/SDP lenses are shown in Fig. 3. All our targets are detected by the *WISE* at 3.4 μm (W1) and 4.6 μm (W2) while at 12 μm (W3) and 22 μm (W4) only SDP.9, SDP.17 and SDP.17 have a counterpart in the *WISE* catalogue. In the following we adopt the *WISE* flux densities determined by standard profile fitting[3] as all our targets have extended source flag *textflg* = 0. For SDP.81 and SDP.130 we use the available 95 per cent upper limit at 12 and 22 μm.

3.4 Spectroscopic redshifts

For all our targets the redshift of the background galaxy has been constrained through the detection of CO emission lines by Z-spec (Lupu et al. 2012), GBT/Zpec (Frayer et al. 2011; Harris et al. 2012), PdBI (N10; George et al., in preparation; Omont et al. 2011, 2013) and CARMA (Leew et al., in preparation). H_2O was detected in SDP.17 (Omont et al. 2011), SDP.9 and SDP.81 (Omont et al. 2013) with PdBI, while emission from [C II] and [O III] has been measured in SDP.81 (Valtchanov et al. 2011). Optical spectra of the foreground galaxy were taken with the William Herschel Telescope (WHT) for SDP.11 and SDP.17 and with the Apache Point Observatory 3.5-m telescope for SDP.130 (N10), giving spectroscopic redshifts in the range $z_{\rm spec} = 0.22$–0.94. For SDP.81 an optical spectrum was already available via SDSS, which gives $z_{\rm spec} = 0.299$. SDP.9 has an optical spectroscopic redshift $z_{\rm spec} = 0.613$ recently obtained with the Gemini-South telescope (Bussmann et al. 2013). A summary of available photometric and spectroscopic information is given in Table 2.

4 LENS SUBTRACTION

According to Figs 1 and 2 (left panels), the *HST* data alone strongly support the idea of a gravitational lensing event in three of the five targets, namely SDP.9, SDP.11 and SDP.17, through the detection of a diffuse ring-like structure around a central elliptical galaxy. Hints of lensing are also found in the WFC3 images of SDP.81, where a faint arclet is visible ∼1.5 arcsec away from the central elliptical galaxy in the west direction. For SDP.130 no clear evidence of gravitational lensing can be claimed from the *HST* images alone, where the system resembles a lenticular galaxy.

In order to unveil the full morphology of the lensed source, the light profile of the foreground galaxy needs to be fitted and subtracted. We use the GALFIT software (Peng et al. 2002) to construct

[3] The *w?mpro* photometry in the Wise All Sky Data Release catalogue, with ? equal to 1, 2, 3 or 4 depending on the observing band.

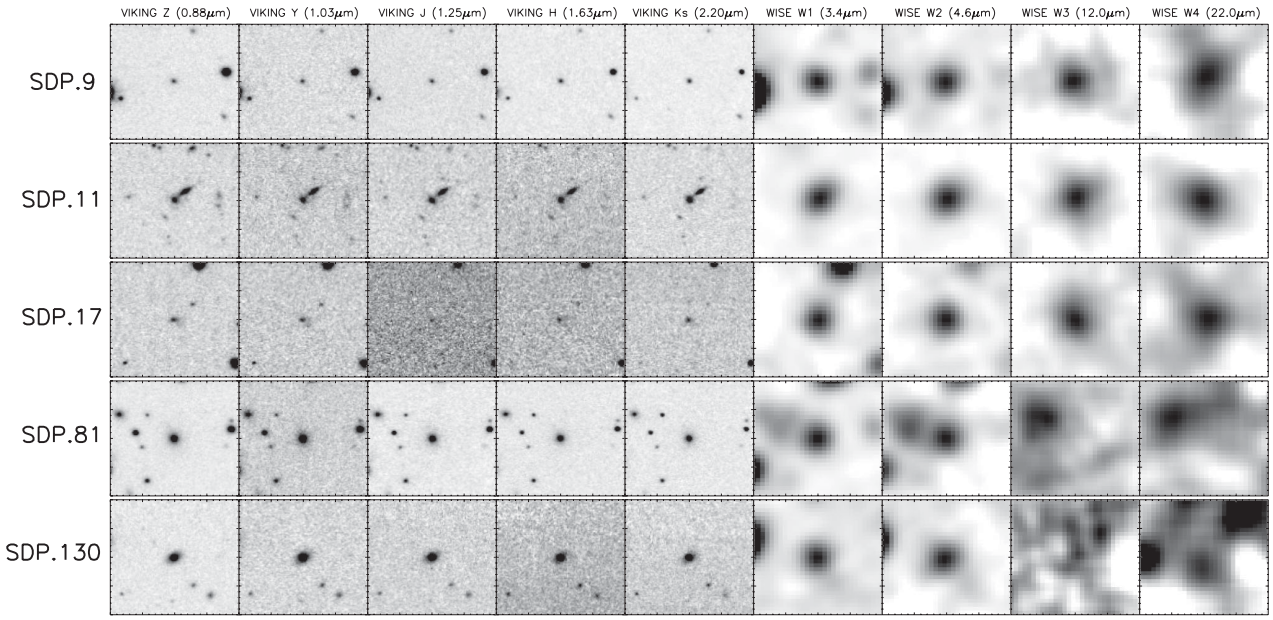

Figure 3. 40 × 40 arcsec^2 postage stamp images of the five H-ATLAS/SDP lensing systems at near- to mid-infrared wavelengths obtained from the VIKING and *WISE* surveys. The stamps are centred at the position of the lensed galaxy.

models of the light profiles for each lensing system. GALFIT performs a non-linear 2D minimization and allows multiple profiles to be simultaneously fitted. As these lensing systems are photometrically blended in the *HST* data, in order to achieve a good fit to the lens galaxy it is necessary to fit profiles to both the lens and source components in the same model. Once a satisfactory model is achieved for the whole system, only the best-fitting lens profile is then subtracted. If there are other sources within the fitting region they are either masked or, if close enough to the main source to cause significant photometric blending, are included in the fit (e.g. the edge-on galaxy at the north-west side of SDP.11; Figs 1 and 2). Where available, sub-arcsecond resolution ancillary data (e.g. from the SMA) are used to guide the fitting process. For each image, nearby stars were combined to give an empirical PSF. All star candidates were checked for saturation, normalized and re-centred before being median combined. For SDP.11 only one suitable star is available.

For each image initially one Sérsic profile was fitted to the foreground lens in order to gauge the level of lensed structure above the detection limit. Then each GALFIT model is built up by adding extra profiles until both the lens and source galaxy components are well represented. The process is iterative and follows the basic loop of applying GALFIT, inspecting the results, adjusting the parameters and possibly adding more complexity where necessary before re-applying GALFIT. This is a process that relies on thorougher visual inspection at each stage, with comparison to other available data, such as the SMA data to check the profiles/model associated with the lensed structure. The fitting process generally started with the higher signal-to-noise ratio F160W image, and then these results used as a prior for the initial guess for F110W. A close eye was kept to try and maintain a reasonable similarity in the profile orientation and ellipticity for both bands, where that was possible. The resulting lens-subtracted images are shown in the right panels of Fig. 2 and compared with the signal-to-noise ratio contours at 880 μm from the SMA (N10; Bussmann et al. 2013). Below we discuss the GALFIT results for the five sources individually.

SDP.9. The foreground galaxy is fitted with a single Sérsic profile of index $n_s = 5.1$ in F110W and $n_s = 5.8$ in F160W. The light profile is therefore consistent with that of an elliptical galaxy. After the subtraction of the lens, a diffuse ring-like structure is clearly revealed, particularly at 1.6 μm. The ring contains two main knots of near-IR emission to the north and south of the lens position and two fainter ones to the east and west.

SDP.11. This is the 500 μm brightest lens candidate selected in the H-ATLAS/SDP field (see Table 2) and even without the subtraction of the foreground galaxy it is clear that the background source is lensed into an Einstein ring. The ring is particularly elongated with a significant amount of substructure, which suggests the presence of several clumps of rest-frame UV/optical emission in the source plane (D14), consistent with what was found for the H-ATLAS lensed galaxy presented in Fu et al. (2012). The foreground galaxy required two Sérsic profiles in each of the bands, where one profile is approximately an exponential disc ($n_s \sim 1$) and the other profile has index $n_s = 2.8$ at 1.1 μm and $n_s = 4.5$ and 1.6 μm. Also in this case the light profile is indicative of an elliptical/lenticular galaxy.

SDP.17. At first glance, this system resembles a face-on spiral galaxy with two prominent spiral arms. However we know from spectroscopic follow-up observations that this system has an optical redshift of 0.9435 (N10) and a redshift of 2.305 from the detection of both CO (Lupu et al. 2012; Harris et al. 2012) and $H_2$0 (Omont et al. 2011) lines, thus indicating the presence of two objects along the same line of sight. Follow-up observations with the SMA (Bussmann et al. 2013) show that the sub-mm/mm emission is relatively compact, concentrated within ∼0.6 arcsec from the centre of the source, but fails to resolve the individual lensed images.

A satisfactory fit to the observed light distribution of this object requires eight profiles as illustrated in Fig. 4: two accounts for the innermost region (i.e. that within $\lesssim$0.3 arcsec from the centre), one with Sérsic index $n_{s,1} \gtrsim 10$ and the another one (less extended) with $n_{s,2} \sim 0.6$ (at both 1.1 and 1.6 μm). We assume that these two profiles describe the foreground galaxy (or at least most of it), which is acting as a lens. The other six profiles may either be all associated

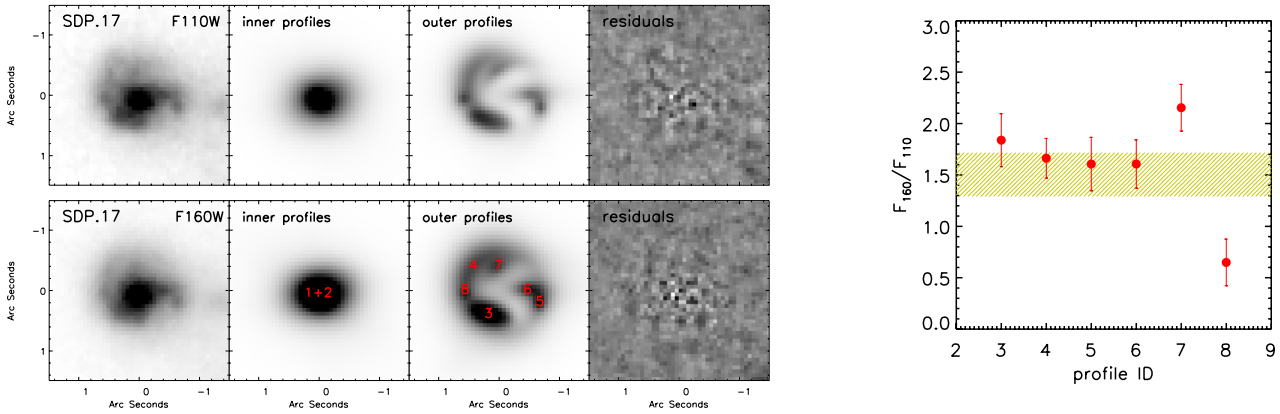

Figure 4. GALFIT results for SDP.17 at 1.1 μm (top panels) and at 1.6 μm (bottom panels). From left to right shown are the input image, the model inner profiles (that we assume describe the lens), the model outer profiles, and the residuals. The 1.6- to 1.1-μm flux density ratios of the outer profiles (marked by numbers in figure) are shown in the right panel and compared with the 1.6- to 1.1-μm flux density ratio of the two inner profiles (yellow shaded region). If the outer profiles are part of the lensed source then their near-IR flux density ratio would increase towards the edges of the image, thus reflecting the reddening of the SED of the background galaxy, due to both high redshift and dust extinction. This is only the case for profile 8. Therefore the background source is assumed to comprise profiles 3−4−5−6−7.

with the lensed source or, at least some of them, may belong to the foreground galaxy. In order to understand the more likely scenario, we have derived the 1.6-μm to 1.1-μm flux density ratio, $F_{1.6}/F_{1.1}$, for each of the outermost profiles. In fact, if the lens had spiral arms then we would expect the arms to display bluer colours than the bulge and the ratio $F_{1.6}/F_{1.1}$ would decrease from the centre towards the outer regions of the galaxy. On the contrary, if the spiral-arms-like structure is part of the lensed source then the same flux density ratio would increase towards the edges of the image, thus reflecting the reddening of the SED of the background galaxy, due to both high redshift and dust extinction (although examples of sub-mm selected galaxies comprising some relatively 'blue' components exist; see e.g. Ivison et al. 2010). The measured flux density ratios are shown in Fig. 4 (right panel). We find that the profile labelled as 8 is significantly bluer than the lens. It might be either another foreground object, not necessarily associated with the lens, or a small star-forming region in the lens itself, which could explain the detection of the lens in CO in the Z-spec spectrum (N10). If it was a dust-free region in the source plane its lensed counter-image would have a similar 1.6-μm to 1.1-μm flux density ratio, but this is not the case. Indeed, all the other outer profiles have either redder colours than the lens (e.g. profile 3 and profile 7) or colours similar to it. Also, if 'blob' 8 was at $z = 2.3$ then the F110W and F160W filters would sample the opposite sides of the Balmer (3646 Å) and the 4000 Å break. Altogether they would give, generally, $F_{1.6}/F_{1.1} > 1.5$ unless the galaxy is very young (i.e. $<10^8$ yr) and dust-free. Therefore the profile labelled as 8 is most likely associated with the foreground galaxy while the other profiles 3−4−5−6−7 are probably suffering some contamination of their colours by the foreground galaxy. In light of these considerations, in this work and in D14 we assume that the lensed object is made up of profiles 3−4−5−6−7.

SDP.81. The fit to the Keck image performed in N10 required two profiles: a compact elliptical Sérsic core plus a subdominant exponential disc. Two Sérsic profiles are required to achieve a good lens subtraction in both *HST* bands, with indexes $n_{s,1} = 2.3$ and $n_{s,2} = 2.0$ for F110W, and $n_{s,1} = 2.9$ and $n_{s,2} = 0.9$ for F160W. Once the lens is subtracted (Fig. 2), two arclets, on opposite sides with respect to the centre of the lens, are revealed. The smaller one, on the west, was barely visible before the subtraction of the lens. The remarkable similarity of the residuals to the structure revealed in the sub-mm by the SMA (see Fig. 2) supports the robustness of the lens fitting procedure.

SDP.130. This system was also fitted in N10 using two profiles: a compact elliptical Sérsic core plus an exponential disc. In the *HST* images the exponential disc is now clearly resolved into two diffuse spiral arms. The lens galaxy can thus be classified as an Sa galaxy. The arm extending in the south-east direction reveals a substructure oriented in an almost orthogonal direction to the arm itself. This small structure produces some emission in the sub-mm (detected with the SMA; Fig. 2) and may suggest that an interaction of the arm with another object is on-going and is triggering some star-formation activity. Another structure is visible close to the bulge, in the north-west direction, but is undetected by the SMA. Its nature is unclear. Overall, the morphology of this system in the *HST* images is not suggestive of a lensing event. This is because, in the near-IR, the lensed object is masked by the prominent bulge of the foreground galaxy. The subtraction of the lens is therefore necessary to reveal the background source.

SDP.130 presents the greatest challenge of the five lenses in terms of subtracting off the lensing galaxy light profile. With the superior resolution of the *HST* images it is now clear that spiral arms are present, although possibly these have suffered some disruption via the interaction with a smaller object (the one to the south-east mentioned before) and now form more of an elongated ring. In addition, there may be a bar structure across the bulge. The GALFIT model of the lens is thus made up of multiple profiles fitted to the bulge, the bar, the spiral arms and the small interacting object. The final model has 16 fitted profiles in all, five associated with the lensing galaxy core, where three profiles represent the bulge and two the bar 'ends'. As shown in Fig. 2, the two profiles representing the lensed structure correspond well to the two most prominent knots seen in the SMA data. Overall SDP.130 is well subtracted.

5 SPECTRAL ENERGY DISTRIBUTIONS

The GALFIT decomposition allows us to measure the photometry of the lensing galaxy and of the background source separately. We use aperture photometry on the GALFIT best-fitting model images to derive the flux densities at 1.1 and 1.6 μm. Photometric errors are

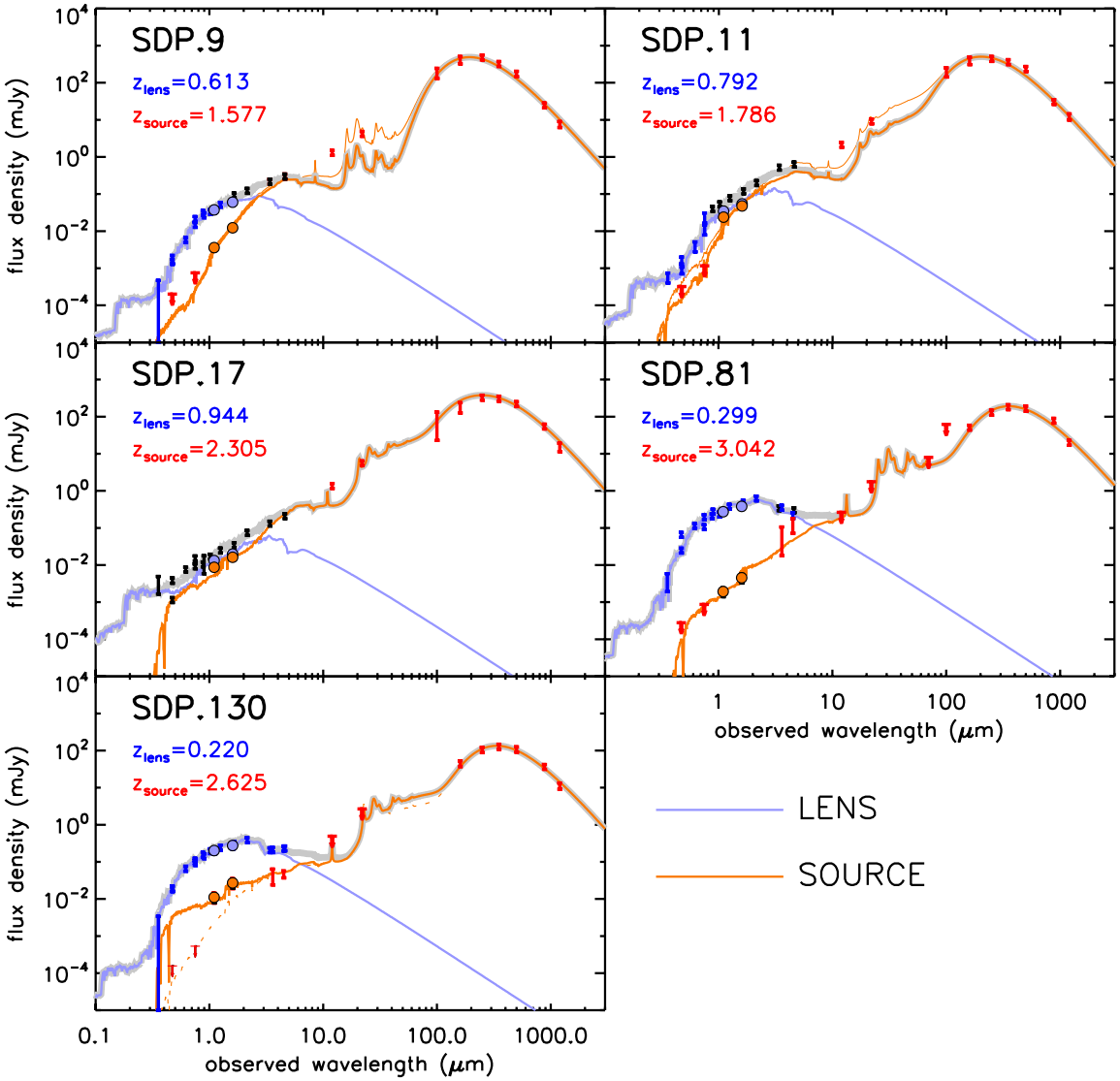

Figure 5. SEDs of the lens and of the background source for the five H-ATLAS/SDP gravitational lensing systems. The new photometric data points from *HST*/WFC3 are indicated by filled circles (cyan for the lens and orange for the background source) while other existing photometric data are represented with either error bars or downward arrows in case of upper limits. The optical data are from SDSS and Keck while measurements at near/mid-IR are from VIKING, *WISE*, and *Spitzer*. The sub-mm/millimetre photometry is from PACS/*Herschel*, SPIRE/*Herschel*, SMA and MAMBO/IRAM. Upper limits at PACS/*Herschel* wavelengths are shown at 3 σ. Data points are blue for the lens photometry, red for the background source photometry and black for the lens+source photometry. The best-fitting SED is in cyan for the lens and in orange for the source. The thick grey line is their sum. For SDP.9 and SDP.11 the lighter orange curve shows the best-fitting results for the lensed source when the *WISE* data points at 12 and 22 μm are included in the fit. For SDP.130, the dashed curve is the best-fitting SED obtained for the lensed source when the Keck upper limits are also taken into account.

obtained by taking aperture photometry of the sky (with the same aperture radius used to measure the flux of the targets) at random positions and estimating the corresponding rms. The results are listed in Table 2 and shown in Fig. 5 (coloured circles: orange for the background source and cyan for the foreground galaxy) together with other available photometric data.

5.1 SED fitting with MAGPHYS

We fit the observed SEDs using the public code Multiwavelength Analysis of Galaxy Physical Properties (MAGPHYS; da Cunha, Charlot & Elbaz 2008), which exploits a large library of optical and IR templates linked together in a physically consistent way. The evolution of the dust-free stellar emission is computed using the population synthesis model of Bruzual & Charlot (2003), by assuming a Chabrier (2003) initial mass function (IMF) that is cutoff below 0.1 and above 100 $M_{\odot}$; adopting a Salpeter IMF instead gives stellar masses that are a factor of ∼1.8 larger.

The attenuation of starlight by dust is described by the two-component model of Charlot & Fall (2000), where dust is associated with the birth clouds and with the diffuse interstellar medium (ISM). Starlight is assumed to be the only significant heating source (i.e. any contribution from an active galactic nucleus is neglected). The dust emission at far-infrared to sub-mm/millimetre wavelengths is modelled as a two modified grey-body SED with dust emissivity index $\beta = 1.5$ for the warm dust (30–60 K) and $\beta = 2$ for the

cold dust (15–30 K). The dust mass absorption coefficient, $k_\lambda \propto \lambda^{-\beta}$, is approximated as a power law with normalization $k_{850\,\mu m} = 0.077\ m^2\ kg^{-1}$ (Dunne et al. 2000).

Among the best SED-fit parameters provided by MAGPHYS we report the following in Table 2: total (3–1000 μm) IR luminosity of dust emission (L_{dust} or L_{IR}), star formation rate (averaged over the last 100 Myr), SFR, stellar mass, M_*, dust mass, M_{dust}, temperature of the warm dust component, $T_{dust}^{(warm)}$, fraction of the IR luminosity due to the warm dust, $\xi_{dust}^{(warm)} = L_{dust}^{(warm)}/L_{dust}$. In order to derive the *intrinsic* properties of the background source, a correction for the amplification due to lensing is applied. We adopt the magnification factors derived by D14 who have modelled the lens-subtracted *HST* images using a multiwavelength semilinear inversion technique (Warren & Dye 2003). The method also provides constraints on the total mass density profile of the lens and on the distribution of the UV/rest-frame optical emission in the source plane. We neglect the effect of differential magnification, i.e. the dependence of the magnification factor on the observing wavelength (Serjeant 2012). In fact, the amplification factors derived by D14 are consistent with those derived for the same objects from the SMA images at 880 μm (Bussmann et al. 2013). Thousands of simulated values for the *observed* MAGPHYS parameters are generated from the likelihood probability distributions provided by MAGPHYS and then divided by the magnification factors randomly drawn from a Gaussian distribution with mean value and rms taken from D14. The medians of the simulated amplification-corrected values are taken as the best estimates of the *intrinsic* properties of the source and are those listed in Table 2. The associated errors correspond to the confidence interval in the 16th to 84th percentile range. We also include in the table the estimates of the molecular gas mass, M_{gas}, which is information provided by Frayer et al. (2011) and Lupu et al. (2012) via the detection of CO emission lines. We have updated their estimates in light of the new amplification factors derived by D14. We also derive the molecular gas fraction, $f_{gas} = M_{gas}/(M_{gas} + M_{star})$ and gas depletion time-scale, $\tau_{gas} = M_{gas}/SFR$, both reported in Table 2.

For the fit to the SED of the background source we adopt the SED templates calibrated to reproduce the ultraviolet-infrared SEDs of local, purely star-forming ULIRGs (da Cunha et al. 2010), while we use dust-free SED templates to fit the SED of the lenses (i.e. pure Bruzual & Charlot 2003 models). For the latter we just report the estimated mass in stars and star formation rate in Table 2.

In general, we assume that the measured SDSS and VIKING photometry have contributions from both the foreground galaxy and the lensed source, unless otherwise stated. In fact, ground based observations are limited by the seeing, which makes it extremely difficult to separate the lens from the background source in our relatively compact targets. We further assume that the emission at 12 and 22 μm (as measured by *WISE*) is entirely contributed by the lensed source while the *WISE* photometry at 3.4 and 4.6 μm carries contributions from both the lens and the source, unless otherwise stated. The best-fitting SED models are shown Fig. 5. Below we provide more details on the fit to the SED for each object individually.

SDP.9. At wavelengths $\lambda \lesssim 1$ μm the emission is dominated by the foreground galaxy. The flux density ratio between the source and the lens increases from 0.08 to 0.2 going from 1.1 μm to 1.6 μm, so that we expect the *H* and *Ks* VIKING photometry to carry significant contributions from both the lens and the background source. Therefore, for the SED of the foreground galaxy we have adopted the SDSS and the $Z + Y + J$ VIKING photometry, as well as the *HST* lens photometry. For the background source, we have fitted the corresponding *HST* photometry, together with $5\,\sigma$ upper limits from Keck in the optical (N10) and all the available data at mid-IR (i.e. *WISE* W3+W4) to sub-mm/mm wavelengths, where the contribution from the lens is null. All the other photometric data are used as upper limits in the fit. The results are shown in the top-left panel of Fig. 5 and are found to be independent on the inclusion of the Keck upper limits. However we fail to reproduce the *WISE* data point at 12 μm (light orange curve). There is a clear excess at mid-IR wavelengths that may be due to emission from a dusty torus around an active galactic nucleus (AGN). The presence of a dust-obscured AGN in SDP.9 is also suggested by the analysis of Omont et al. (2011) on the $H_2O(2_{02}1_{11})$/CO(8-7) and $I(H_2O)/L_{FIR}$ ratios. Our SED models do not include any AGN component, which may provide the dominant contribution to the continuum mid-IR emission. Therefore we assume as our best-fitting SED model the one derived by ignoring the *WISE* W3+W4 data points (thick orange curve). The effect of the AGN on the derived best-fitting MAGPHYS parameters is discussed in Section 5.2.

According to D14 the source is amplified by a factor $\mu = 6.3$ and consists of a dominant emitting region of ∼1 kpc in size, and a smaller and fainter one separated by a few kpc. The latter is responsible for the fainter structure observed in the Einstein ring. The background source has a mass in stars $M_* = 7.1 \times 10^{10}\,M_\odot$, a comparable mass in molecular gas, $M_{gas} = 3.4 \times 10^{10}\,M_\odot$, and form stars at a rate of $366\,M_\odot\ yr^{-1}$.

SDP.11. The foreground galaxy and the lensed source have about the same flux densities at near-IR wavelengths. This means that lower spatial resolution near-IR photometric data, as those provided by the VIKING survey, may carry similar contributions from the lens and the background source, although the two are completely blended together. Based on the available upper limits at optical wavelengths for the lensed source we decided to use the $u + g + r + i$ SDSS photometry as well as the *HST* lens photometry to describe the SED of the foreground galaxy, while the fit to the SED of the lensed galaxy is performed on the *Keck* upper limits, the *HST* source photometry and on photometric data at wavelengths > 10 μm. However, also in this case we fail to reproduce the *WISE* W3 data point (light orange curve). We conclude that a significant fraction of the mid-IR emission in SDP.11 may come from an AGN (see discussion in Section 5.2). As for SDP.9, we assume as our best-fitting SED model the one derived by ignoring the *WISE* W3+W4 data points (thick orange curve).

The magnification factor derived by D14 for the background galaxy is $\mu = 7.9$. The reconstructed source comprises several knots of rest-frame optical emission, distributed within a region of a few kpc, which are responsible for the small-scale structure observed in the Einstein ring (D14). Compared to SDP.9, the source has a higher star formation rate, SFR $\sim 650\,M_\odot\ yr^{-1}$, a higher mass in stars $M_* = 1.9 \times 10^{11}\,M_\odot$, and a lower gas fraction, $f_{gas} = 0.14$.

SDP.17. This case is similar to that of SDP.11 with the foreground galaxy and the lensed source having very similar flux densities at near-IR wavelengths. Therefore we fit the SED of the lens including just the *HST* lens photometry and adopting the SDSS data points as upper limits. We fit similarly for the lensed source with the addition of the photometric data at wavelengths longwards of 10 μm. No indication of a mid-IR 'excess' is found in this case.

The background galaxy is affected by a small amplification, $\mu = 3.6$ (D14). Given its relatively high redshift and high 500 μm flux density, the source is the brightest among the lensed galaxies in the sample, with an infrared luminosity exceeding $10^{13}\,L_\odot$. There are two distinct objects in the source plane, each one of 2–3 kpc

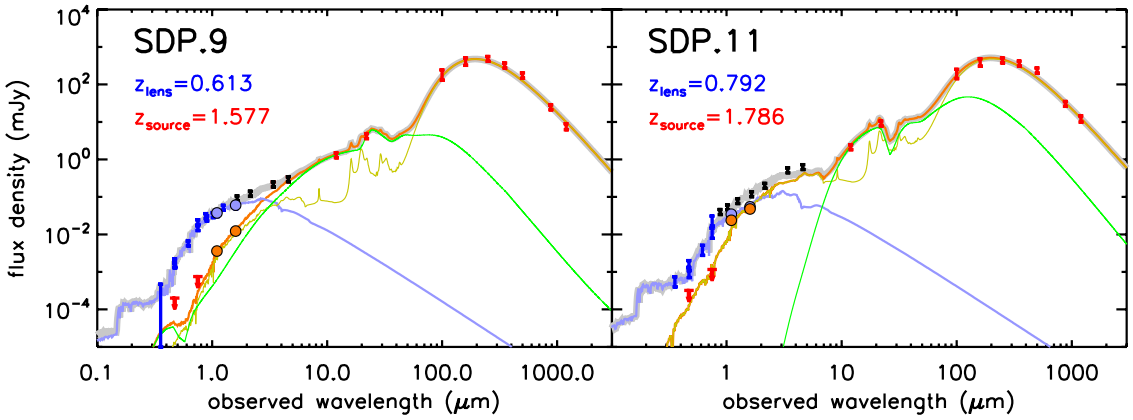

Figure 6. Same as in Fig. 5 for SDP.9 and SDP.11 but with the inclusion of an AGN component, represented by the green curve. The star-forming component, as derived from MAGPHYS, is shown in yellow. The orange curve is the sum of the star-forming and the AGN components.

in size, and separated by a few kpc (D14). This morphology may be indicative of an on-going merger. The background system has SFR $\sim 2300\,M_\odot\,yr^{-1}$ and $M_* \sim 2.4 \times 10^{11}\,M_\odot$. The mass in molecular gas is $M_{gas} = 5.9 \times 10^{10}\,M_\odot$, corresponding to a gas fraction of 20 per cent.

SDP.81. The foreground galaxy completely dominates the emission at wavelengths shorter than a few μm. Therefore the fit to the SED of the lens is done on the SDSS and VIKING data, as well as on the lens photometry from *HST* and *Spitzer* (Hopwood et al. 2011). As for the background galaxy, we fit upper limits from Keck, source photometry from *HST* and *Spitzer* and all the other available photometric data above 10 μm.

The background galaxy is amplified by a factor $\mu = 11$, the highest among those derived by D14. The lensed system resembles a classic cusp-caustic configuration and the reconstructed source shows little structure other than a slight elongation. The background galaxy has SFR $= 527\,M_\odot\,yr^{-1}$ and $M_* = 3.3 \times 10^{10}\,M_\odot$, with a gas fraction of 33 per cent.

SDP.130. The lensed galaxy is an order of magnitude fainter than the foreground galaxy at 1.1 and 1.6 μm. On the other hand the complicated morphology of the foreground galaxy may suggest that the upper limits available at optical wavelengths for the lensed source are poorly constrained. In fact, we failed to reproduce simultaneously those limits and the *HST* photometry (dashed curve), as the increase in flux density from 0.7 to 1.1 μm is too steep. Therefore we also show in Fig. 5 the best-fitting SED model derived when the Keck upper limits are not included in the fit (thick orange curve). The latter is assumed as our best-fitting SED model for the background galaxy.

As for SDP.17, the amplification is relatively small, $\mu = 3.1$ (D14). The source extends over several kpc and there is a hint of substructures (two main knots of emission) from the reconstructed F160W image (D14). The background galaxy has infrared luminosity close to $10^{13}\,L_\odot$ and $SFR = 1026\,M_\odot\,yr^{-1}$. The mass in stars exceeds $10^{11}\,M_\odot$, while that in molecular gas is $5.3 \times 10^{10}\,M_\odot$, corresponding to a gas fraction of 28 per cent.

5.2 Effect of the AGN on the estimated MAGPHYS parameters

The 'excess' emission at mid-IR wavelengths observed in SDP.9 and SDP.11 suggests the presence of a buried AGN, which may have an impact on the MAGPHYS results presented in Table 2. A way to investigate this effect is to fit the observed SED with a combination of AGN and star-forming templates (e.g. Negrello et al. 2009; Berta et al. 2013; Delvecchio et al. 2014). However this approach may lead to large degeneracies between model parameters when the spectral coverage is not sufficiently good, as it is the case here. In fact, only few constraints on the SED of the background galaxy are available at optical and near-IR wavelengths. For this reason we have adopted a simpler approach. We have assumed that the mid-infrared emission is completely dominated by the AGN and fitted the *WISE* W3 and W4 photometry with a suitable set of AGN templates. The photometric data points at optical/near-IR/far-IR/sub-mm/mm wavelengths are taken as upper limits in the fitting process. We have exploited the library[4] of AGN templates provided by Fritz, Franceschini & Hatziminaoglou (2006), and further expanded by Feltre et al. (2012). The AGN library includes 2400 templates, obtained by varying the torus opening angle, the radial and the height slope of the torus density profile, the equatorial optical depth at 9.7 μm, the ratio between the outer and inner radius of the dust distribution and the viewing angle of the line of sight. Once the best-fitting AGN template is found, the latter is subtracted from the observed SED and the residuals are fitted again with MAGPHYS. Where the residuals are consistent with zero (i.e. in the W3 and W4 bands) $3\,\sigma$ upper limits are assumed, σ being the error on the measured photometry at that wavelength. The new SED fit results are shown in Fig. 6. In general, the contribution of the AGN is confined to the mid-IR spectral region, although in SDP.9 it also extends to near-IR wavelengths where the AGN accounts for about 20 per cent of the measured flux density at 1.6 μm. The overall effect on the newly derived MAGPHYS parameters is to decrease the infrared luminosities and the star formation rates (as well as the mass in stars for SDP.9) compared to the values quoted in Table 2. However, as expected, the differences are not significant (i.e. well within the 1σ uncertainties). In fact the measured *WISE* W3 and W4 photometry was significantly underestimated by the best-fitting MAGPHYS template even before the AGN component was included in the fit.

6 DISCUSSION

All the galaxies in the sample are classified as Ultra Luminous Infrared Galaxies (ULIRGs; $10^{12}\,L_\odot \leq L_{IR} < 10^{13}\,L_\odot$) with the exception of SDP.17; its infrared luminosity, $L_{IR} \sim 2 \times 10^{13}\,L_\odot$,

[4] The templates are publicly available and can be downloaded from http://users.ugent.be/~jfritz/jfhp/TORUS.html

makes it a Hyper Luminous Infrared Galaxy (HyLIRGs). SDP.17 is not the first example of HyLIRG discovered among the H-ATLAS lens candidates. Other examples are the $z = 4.243$ lensed galaxy analysed by Cox et al. (2011) and further investigated by Bussmann et al. (2012), the $z = 3.259$ source lensed by a galaxy group discussed in Fu et al. (2012), and the two star-bursting galaxies (one of which is weakly lensed) at $z = 2.41$ presented by Ivison et al. (2013). A few more examples have been found in the *Herschel* Multi-tiered Extragalactic Survey(HerMES; Oliver 2012): a $z = 2.9575$ source lensed by a galaxy group (Conley et al. 2011) and a weakly lensed merging system at $z = 2.308$ (Fu et al. 2013).

The inferred star formation rates are in the range $\gtrsim$400–2000 $M_\odot$ yr^{-1}, reaching a maximum for SDP.17 and SDP.130. The derived dust masses, $M_{\rm dust} \sim (7–30) \times 10^8\,M_\odot$ and dust temperatures, $T = 37–47$ K, are in agreement with what is commonly found for high-redshift ULIRGs/HyLIRGs (Michałowski, Hjorth & Watson 2010; Bussmann et al. 2013). At these high rates of star formation, the mass in stars grows very rapidly as the available molecular gas is quickly exhausted. With the aid of the new *HST* photometry we estimate that a mass of $\sim(7–20) \times 10^{10}\,M_\odot$ is already locked up in stars. Although high, these values are a factor of $\times 4$ lower than those derived by Hopwood et al. (2011) for SDP.81 and SDP.130. In fact, their SED fitting could only rely on upper limits for the flux density of the lensed source at wavelengths $\lambda < 3.6\,\mu$m. Our estimates of the mass in stars are consistent with those derived for other sub-millimetre selected galaxies (Michałowski et al. 2010; Hainline et al. 2011; Yun et al. 2012, see also Fig. 7).

For how long will these galaxies continue to form stars? This depends on the mass of molecular gas, $M_{\rm gas}$, still available in these sources. We find large reservoir of molecular gas, $M_{\rm gas} > 3 \times 10^{10}\,M_\odot$, consistently with what is observed in other sub-millimetre galaxies (Bothwell et al. 2013, in Fig. 7). If star formation is sustained at the rate estimated here, the gas will be exhausted in less than 100 Myr ($\times 2$ longer if gas recycling is accounted for in stellar evolution; Fu et al. 2013). By the end of this intense episode of star formation such galaxies will have assembled a mass in stars of $(1–3) \times 10^{11}\,M_\odot$. Unless further gas is accreted from the surrounding environment or through minor/major mergers, they will passively evolve into massive ellipticals at the present time. These galaxies are thus proto-ellipticals caught during their major episode of star formation.

Evidence for the presence of an AGN have been found in two sources (SDP.9 and SDP.11). The inferred AGN bolometric luminosities (corrected for lensing) are $1.3 \times 10^{12}\,L_\odot$ for SDP.9 and $1.1 \times 10^{13}\,L_\odot$ for SDP.11, although these may be overestimated. In fact, due to the smaller size of the emitting region, the *apparent* AGN luminosity is probably affected by a higher magnification than that derived from imaging data at near-IR and sub-mm wavelengths. The emerging of an AGN is expected during the final stage of the evolution of massive forming spheroids at $z \gtrsim 1.5$ as a mechanism to quench the star formation and to account for the *cosmic downsizing* (see e.g. Granato et al. 2004, and references therein). In their recently proposed model for the co-evolution of supermassive black holes and their host galaxies, Lapi et al. (2014) have shown that the ratio $L_{\rm FIR}/L_{\rm AGN}$ between the far-infrared luminosity (i.e. luminosity integrated in the rest-frame wavelength range 40 μm–500 μm) and the AGN bolometric luminosity characterizes the time evolution of the galaxy plus AGN system; it is a decreasing function of the galactic time and marks the evolution from the epoch when the luminosity budget is dominated by the star formation ($L_{\rm FIR}/L_{\rm AGN} > 1$) to the epoch when the AGN/QSO takes over ($L_{\rm FIR}/L_{\rm AGN} < 1$). This ratio is $\sim$4 for SDP.9 and $\sim$0.5 for SDP.11, suggesting that in the former the central black hole is still in his early phase of mass accretion, while in the latter the black hole has reached its final mass and the AGN feedback is about to quench the star formation and to stop the inflow of gas towards the centre of the galaxy. According to Lapi et al. the central black hole grows exponentially from a seed of $\lesssim 10^4\,M_\odot$, with a luminosity close to (or slightly above) the Eddington luminosity. The e-folding time-scale of the black hole growth is $\sim$70 Myr, assuming a mass to radiation conversion efficiency $\epsilon = 0.15$. Therefore, it would take about 8 (for SDP.9) to 12 (for SDP.11) e-folding times (i.e. $\sim$550−850 Myr) for the AGN to reach the observed bolometric luminosity starting from $M_{\rm BH} = 10^4\,M_\odot$. This value is consistent, within the (large) uncertainties, with the age of the sources derived from the measured mass in stars and SFR (assuming the SFR is kept constant during the starburst event), i.e.: $M_\star/{\rm SFR} = 467^{+492}_{-371}$ Myr for SDP.9 and $M_\star/{\rm SFR} = 382^{+597}_{-141}$ Myr for SDP.11.

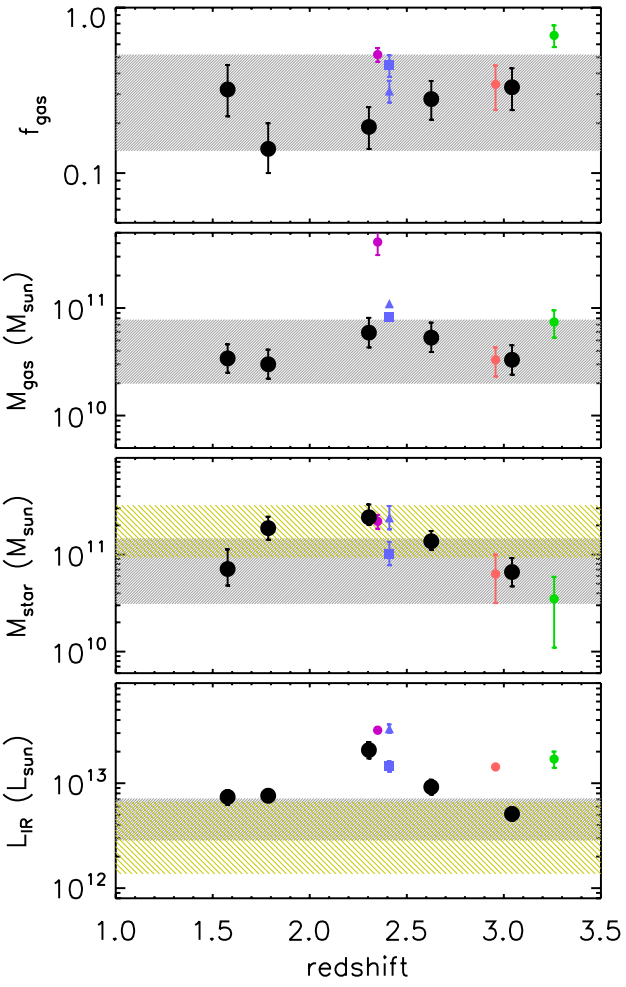

Figure 7. Infrared luminosity, mass in stars, mass in molecular gas and gas fraction of the five H-ATLAS/SDP lensed galaxies (black dots) compared with other sub-mm selected lensed/un-lensed galaxies from literature: Ivison et al. (2013; cyan), Fu et al. (2012; green), Conley et al. (2011; red), Fu et al. (2013; purple). The shaded grey region corresponds to the 16th to 84th percentile range of the distribution of values derived for the sample of sub-millimetre galaxies with CO line measurements compiled by Bothwell et al. (2013; with mass in stars taken from Hainline et al. 2011). The shaded yellow region shows the infrared luminosities and masses in stars estimated by Michałowski et al. (2010; their values of M_* have been rescaled by a factor of 1.8 to convert from Salpeter to Chabrier initial mass function.)

7 CONCLUSIONS

We have presented deep *HST*/WFC3 F110W+F160W follow-up observations of the first gravitational lensing systems discovered by H-ATLAS in the SDP. The exquisite angular resolution of the *HST* images has allowed us to resolve an Einstein ring in two of these systems, and to identify multiple images in the others after a careful removal of the foreground galaxy. The lens-subtracted images have been used to model the rest-frame UV/optical emission in the source plane (D14) and to improve the constraints on the mass in stars and on other physical properties of lensed galaxies via SED fitting. Our conclusions can be summarized as follows:

(i) The background sources comprise a mixture of ULIRGs and HyLIRG with star formation rates SFR $\sim$ 400–2000 $M_\odot$ yr^{-1}, and large dust masses, $M_{\rm dust} = (7-30) \times 10^8\,M_\odot$. SDP.11 and SDP.17 are resolved into multiple knots of rest-frame UV/optical emission in the source plane (D14) indicative of either a major merger (Fu et al. 2013) or distinct clumps of star formation within the same proto-galaxy (Swinbank et al. 2011).

(ii) The lensed galaxies have already assembled a mass in stars $M_* = (6\text{–}25) \times 10^{10}\,M_\odot$. Their molecular gas content is still significant, $f_{\rm gas} \sim 15$–30 per cent, so that star formation can be sustained for another $\lesssim$100 Myr at the inferred rate.

(iii) By the end of their star formation activity all these galaxies will have a mass in stars $\gtrsim 10^{11}\,M_\odot$. We are thus witnessing the very early stages in the formation of elliptical galaxies, during the peak epoch ($z \sim 1.5$–3) of the cosmic star formation history of the Universe.

(iv) There is indication of the presence of an AGN in two of the lensed systems. The observed emission at mid-infrared wavelengths, in excess to that expected from purely star-forming SEDs, is a signature of the growth of the central black hole in these proto-ellipticals, as predicted by models for the co-evolution of supermassive black holes and their host galaxies (e.g. Lapi et al. 2014, and references therein).

The wide range of lens-to-source flux density ratios at 1.1- and 1.6-μm observed in this sample suggests that, in some cases, the lensed source may significantly contribute to the near-IR photometry of the system, as measured in low angular resolution VIKING and *WISE* surveys. Therefore, sub-mm lens candidates showing an 'excess' of emission at near-IR wavelengths compared to that expected for a passively evolving elliptical (i.e. the lens) are ideal targets for successful follow-up observations in the near-IR with *HST*/WFC3 and with the Keck telescopes (in Adaptive Optics), aiming at spatially resolving the lensed structure in these systems (Gonzalez-Nuevo et al. 2012). Many more lens candidates from both H-ATLAS and HerMES have been now observed with *HST*/WFC3/F110W in cycle-19 (PID: 12488) and with Keck/AO in the *H* and *K* bands. Lens modelling and SED fitting for these targets will be presented in a series of upcoming papers (Amber et al., in preparation; Calanog et al., in preparation).

ACKNOWLEDGEMENTS

This work was supported by STFC (grants PP/D002400/1 and ST/G002533/1), by ASI/INAF agreement I/072/09/0, by PRIN-INAF 2012 project 'Looking into the dust-obscured phase of galaxy formation through cosmic zoom lenses in the Herschel Astrophysical Large Area Survey' and, in part, by the Spanish Ministerio de Ciencia e Innovacion (project AYA2010-21766-C03-01). JGN acknowledges financial support from the Spanish CSIC for a JAE-DOC fellowship, co-funded by the European Social Fund. *Herschel* is an ESA space observatory with science instruments provided by European-led Principal Investigator consortia and with important participation from NASA. The *Herschel*-ATLAS is a project with *Herschel*, which is an ESA space observatory with science instruments provided by European-led Principal Investigator consortia and with important participation from NASA. The H-ATLAS website is http://www.h-atlas.org/. This publication makes use of data products from the *WISE*, which is a joint project of the University of California, Los Angeles, and the Jet Propulsion Laboratory/California Institute of Technology, funded by the National Aeronautics and Space Administration.

REFERENCES

Baes M. et al., 2010, A&A, 518, 39
Berta S. et al., 2013, A&A, 551, 100
Bothwell M. S. et al., 2013, MNRAS, 429, 3047
Bruzual G., Charlot S., 2003, MNRAS, 344, 1000
Bussmann S. et al., 2012, ApJ, 756, 134
Bussmann S. et al., 2013, ApJ, 779, 25
Chabrier G., 2003, PASP, 115, 763
Charlot S., Fall S. M., 2000, ApJ, 539, 718
Conley A. et al., 2011, ApJ, 732, 35
Coppin K. et al., 2006, MNRAS, 372, 1621
Cox P. et al., 2011, ApJ, 740, 63
da Cunha E., Charlot S., Elbaz D., 2008, MNRAS, 388, 1595
da Cunha E., Charmandaris V., D´az-Santos T., Armus L., Marshall J. A., Elbaz D., 2010, A&A, 523, A78
Delvecchio I. et al., 2014, MNRAS, in press
Devlin M. J. et al., 2009, Nature, 458, 737
Dunne L., Eales S., Edmunds M., Ivison R., Alexander P., Clements D. L., 2000, MNRAS, 315, 115
Dye S. et al., 2014, MNRAS, in press (D14)
Eales S. et al., 2010a, PASP, 122, 499
Eales S. et al., 2010b, A&A, 518, L23
Feltre A., Hatziminaoglou E., Fritz J., Franceschini A., 2012, MNRAS, 426, 120
Fleuren S. et al., 2012, MNRAS, 423, 2407
Frayer D. et al., 2011, ApJ, 726, L22
Fritz J., Franceschini A., Hatziminaoglou E., 2006, MNRAS, 366, 767
Fu H. et al., 2012, ApJ, 753, 134
Fu H. et al., 2013, Nature, 498, 338
Gonzalez-Nuevo J. et al., 2010, A&A, 518, 38
Gonzalez-Nuevo J. et al., 2012, ApJ, 749, 65
Granato G. L., De Zotti G., Silva L., Bressan A., Danese L., 2004, ApJ, 600, 580
Griffin M. J. et al., 2010, A&A, 518, L3
Gruppioni C. et al., 2013, MNRAS, 432, 23
Hainline L. J., Blain A. W., Alexander D. M., Armus L., Chapman S. C., Ivison R. J., 2011, ApJ, 740, 96
Harris A. et al., 2012, ApJ, 752, 152
Hopwood R. et al., 2011, ApJ, 728, L4
Ibar E. et al., 2010, MNRAS, 409, 38
Ivison R. J., Smail I., Papadopoulos P. P., World I., Richard J., Swinbank A. M., Kneib J. P., Owen F. N., 2010, MNRAS, 404, 198
Ivison R. J. et al., 2013, ApJ, 772, 137
Lapi A., Shankar F., Mao J., Granato G., Silva L., De zotti G., Danese L., 2006, ApJ, 650, 42
Lapi A. et al., 2011, ApJ, 742, 24
Lapi A. et al., 2014, ApJ, 782, 69
Lupu R. et al., 2012, ApJ, 757, 135
Michałowski M., Hjorth J., Watson D., 2010, A&A, 514, A67
Negrello M. et al., 2007, MNRAS, 377, 1557
Negrello M. et al., 2009, MNRAS, 394, 375
Negrello M. et al., 2010, Science, 330, 800 (N10)

Oliver S. J. et al., 2012, MNRAS, 424, 1614
Omont A. et al., 2011, A&A, 530, 30
Omont A. et al., 2013, A&A, 551, A115
Pascale E. et al., 2010, MNRAS, 415, 911
Peng C. Y., Ho L. C., Impey C. D., Rix H.-W., 2002, AJ, 124, 266
Pilbratt G. et al., 2010, A&A, 518, 1
Poglitsch A. et al., 2010, A&A, 518, L2
Rigby E. et al., 2011, MNRAS, 415, 2336
Serjeant S., 2012, MNRAS, 424, 2429
Smith D. et al., 2011, MNRAS, 416, 857
Swinbank M. et al., 2011, ApJ, 742, 11
Valtchanov I. et al., 2011, MNRAS, 415, 3473
Wardlow J. et al., 2013, ApJ, 762, 59
Warren S., Dye S., 2003, ApJ, 590, 673
Weiss A. et al., 2009, ApJ, 707, 1201
Wright E. L. et al., 2010, AJ, 140, 1868
Yun M. S. et al., 2012, MNRAS, 420, 957

[1]*INAF, Osservatorio Astronomico di Padova, Vicolo Osservatorio 5, I-35122 Padova, Italy*
[2]*Imperial College London, Blackett Laboratory, Prince Consort Road, London SW7 2AZ, UK*
[3]*School of Physics and Astronomy, University of Nottingham, University Park, Nottingham NG7 2RD, UK*
[4]*Max Planck Institute for Astronomy, Koenigstuhl 17, D-69117 Heidelberg, Germany*
[5]*Department of Physical Sciences, The Open University, Walton Hall, Milton Keynes MK7 6AA, UK*
[6]*Sterrenkundig Observatorium, Universiteit Gent, Krijgslaan 281 S9, B-9000 Gent, Belgium*
[7]*(SUPA) School of Physics & Astronomy, University of St Andrews, North Haugh, St Andrews, KY16 9SS, UK*
[8]*School of Mathematical Sciences, Queen Mary, University of London, Mile End Road, London E1 4NS, UK*
[9]*Harvard–Smithsonian Center for Astrophysics, 60 Garden Street, Cambridge, MA 02138, USA*
[10]*Department of Astronomy, Space Science Building, Cornell University, Ithaca, NY 14853-6801, USA*
[11]*Department of Physics & Astronomy, University of California, Irvine, CA 92697, USA*
[12]*Institut fur Astronomie, Universitat Wien, Turkenschanzstrae 17, A-1160 Wien, Austria*
[13]*Instituto de Fisica de Cantabria (CSIC-UC), Avda. los Castros s/n, E-39005 Santander, Spain*
[14]*Dipartimento di Fisica, Universita' Tor Vergata, Via della Ricerca Scientifica 1, I-00133 Roma, Italy*
[15]*Astrophysics Sector, SISSA, Via Bonomea 265, I-34136 Trieste, Italy*
[16]*UPMC Univ. Paris 06, UMR7095, Institut d'Astrophysique de Paris, 75014 Paris, France*
[17]*CNRS, UMR7095, Institut d'Astrophysique de Paris, F-75014 Paris, France*
[18]*School of Physics and Astronomy, Cardiff University, The Parade, Cardiff CF24 3AA, UK*
[19]*Observatoire de Genève, Université de Genève, 51 Ch. des Maillettes, CH-1290 Versoix, Switzerland*
[20]*Department of Physics and Astronomy, University of Canterbury, Private Bag 4800, Christchurch, New Zealand*
[21]*Instituto de Física y Astronomía, Universidad de Valparaíso, Avda. Gran Bretaa 1111, Valparaíso, Chile*
[22]*European Southern Observatory, Karl Schwarzschild Strasse 2, D-85748 Garching, Germany*
[23]*Scottish Universities Physics Alliance, Institute for Astronomy, University of Edinburgh, Royal Observatory, Edinburgh EH9 3HJ, UK*
[24]*Departamento de Astronomia y Astrofisica, Universidad Catolica de Chile, Vicuna Mackenna 4860, Casilla 306, Santiago 22, Chile*
[25]*College of Graduate Studies, UNISA, P. O. Box 392, UNISA, 0003, South Africa*
[26]*INAF, Istituto di Radioastronomia, Via Gobetti 101, I-40129 Bologna, Italy*
[27]*Leiden Observatory, PO Box 9513, NL-2300 RA Leiden, The Netherlands*
[28]*Centre for Astrophysics Research, Science & Technology Research Institute, University of Hertfordshire, Herts AL10 9AB, UK*
[29]*Astrophysics Branch, NASA/Ames Research Center, MS 245-6, Moffett Field, CA 94035, USA*

This paper has been typeset from a TEX/LATEX file prepared by the author.